A proton sensor for energies from 2MeV to 20MeV

Marine Ruffenach, Sébastien Bourdarie, Julien Mekki, Didier Falguère, Jean-Roch Vaillé, Jérôme Carron, Philippe Bourdoux, Louis Nguyen

A proton sensor for energies from 2MeV to 20MeV

M. Ruffenach, S. Bourdarie, J. Mekki, D. Falguère, J. Vaillé, J. Carron, P. Bourdoux, and L. Nguyen

***Abstract*—CNES and ONERA have developed a radiation monitor ICARE-NG (Influence sur les Composants Avancés des Radiations de l'Espace-Nouvelle Génération) to measure protons and electrons in radiation belts. This instrument is able to measure a wide range of energy for protons and electrons, but no measurements of few MeV protons are performed. The objective of this study is to extend capabilities of this radiation monitor by adding a low-energy proton sensor. In this article the design of a sensor for low-energy protons compatible with the ICARE-NG instrument is presented. Response functions for protons and electrons of the low-energy proton sensor are calculated using Monte-Carlo simulations. The calculation of predicted count rates of particles are performed. The manufacturing of the instrument as well as tests are discussed.**

***Index Terms*—Geant4, Monte-Carlo simulations, proton, radiation belts, radiation monitor, response function, space environment.**

I. Introduction

Due to the magnetic field of the Earth, protons and electrons are trapped in a restricted region of the magnetosphere and constitute radiation belts [1]. A good knowledge of these regions is mandatory to prevent damage on satellites or even their loss [2]. While a bunch of measurements of proton flux with energies greater than 10 Megaelectron-Volts (MeV) are available [3] [4] [5] [6], in-situ measurements of 1-10 MeV protons are not common. These protons are responsible for solar array degradation. The challenge to have good measurements of low-energy protons is to accurately discriminate protons with energy of a few MeV from protons with energy of several tens of MeV, and from energetic electrons. Such monitors have already been developed: MEPED [7], LPT [8], SST [9], RBSPICE [10], and MagEIS [11]. The aim of this study is to design a sensor of low-energy protons compatible with the existing ICARE-NG instrument which flew over several missions as Jason-2 [3] and SAC-D (Satelite de Aplicaciones Cientificas-D) [4]. Valid proton energy range measured by ICARE-NG on Jason-2 and SAC-D is from 12.8 MeV to 190 MeV. Such a new sensor will extend this energy range down to 2 MeV protons.

In section II, a brief presentation of the ICARE-NG instrument and the geometry of the low-energy proton sensor are given. In section III the modelling of the sensor is described. In particular, it focuses on numerical results of response functions of the sensor and the modelling of predicted count rates of particles. In this section, saturation and total counts are also discussed. The manufacturing of the instrument and tests that will be performed are discussed in section IV. Finally, conclusions are given in section V.

II. The instrument's geometry

The ICARE instrument was developed at the end of the 90s and has flown on the MIR space station, the International Space Station and SAC-C spacecraft [12]. An updated version of the instrument, ICARE-NG, was developed in the 2000s. It has been implemented on Jason-2 [3], Jason-3 [13], SAC-D [4], and recently on Eutelsat 7C spacecraft. The ICARE-NG instrument consists of three sensors (A, B, and C). Both sensors A and C are set to primarily measure protons while sensor B measures electrons. Particle fluxes for electrons from 250 keV to 3.2 MeV and for protons from 12.8 MeV to 190 MeV are available. A complete description of the ICARE-NG instrument can be found in [3].

To expand instrument capabilities, it was decided to develop a new low-energy proton sensor (2-20 MeV), with no impact on electronics or mechanical design. In order to keep electron measurements available, sensor B must not be modified. Therefore, the best compromise is to be able to implement either the actual sensor C or the new low-energy proton sensor. The geometry of the low-energy proton sensor has to satisfy several objectives: (1) an accurate discrimination of ionizing particles in a mixed field must be guaranteed, (2) it must be compatible with the existing ICARE-NG electronics design, and (3) it must be compatible with the actual mechanical design of ICARE-NG. Satisfying the second constraint requires implementation of a sensor based on solid state detectors with coincidence and anti-coincidence modes and to measure energy deposition in the 0-12 MeV range approximatively. Deposited energies are digitized throughout 256 channels linearly spaced in energy from 0 MeV to 12 MeV by a pulse-height analyzer. The diodes in the new sensor have to be at the same locations as in sensor C. The bias voltage applied is around 100 V so that silicon diodes are fully

Manuscript received November 29, 2019; revised January 6, 2020; accepted December 14, 2019.

This work was conducted as part of a co-financing of doctoral thesis research CNES N° 17054 - ONERA N° 9218.

M. Ruffenach, S. Bourdarie and D. Falguère are with The French Aerospace Lab/Département Physique Instrumentation Environnement et Espace, ONERA, 31055 Toulouse, France (e-mail: marine.ruffenach@onera.fr).

J. Mekki and J. Carron are with CNES, 31401 Toulouse, France.

J.R. Vaillé is with IES – UMR UM/CNRS 5214, Université de Montpellier, 34097 Montpellier, France.

P. Bourdoux and L. Nguyen are with EREMS, 31130 Flourens, France.

depleted. In anti-coincidence mode, particles which deposit energy only in the first diode are considered while in coincidence mode particles which deposit energy in the two diodes are registered. For the coincidence mode, the total energy deposited in both diodes is divided by a factor of 2 to have the same range of deposited energy for the two modes. This is necessary for the pulse-height analyzer. The third objective means that the size of the sensor is limited in terms of dimension and weight. Therefore, the volume of the new sensor is limited by other sensors, i.e., the thickness of the shielding must be roughly the same as for sensor C. The first objective is much more challenging: for example, in a 700 µm thick silicon diode a 1 MeV proton can deposit the same amount of energy as a 100 MeV proton or a 1 MeV electron. So, the first challenge to face is to reduce the contribution of electrons and high-energy protons in order to get accurate measurements of low-energy protons. To reduce the contribution of high-energy protons while the shielding thickness must not exceed that of sensor C, a shielding made of tungsten is chosen. However, the production of Bremsstrahlung depends on the square of the atomic number of the target so the tungsten fosters this phenomenon. The Bremsstrahlung depend also on the energy of the incident electron so to minimize this effect aluminum is added on both sides of the tungsten shielding. It allows reducing the energy of electrons before they reach the tungsten. At the main entrance of the sensor, a samarium-cobalt magnet is used to deflect the major part of electrons incoming by the aperture before they reach the first silicon diode. Because protons are heavier, they are not affected in the energy range of interest (few MeV). The magnet is described in section III. Note that aluminum baffles are used to attenuate the scattering of particles in the collimator. To make sure the magnetic field produced by the magnet will not impact measurements made by the two other sensors, a steel strapping is used to confine the magnetic field inside the sensor. Finally, diameters of diodes are chosen so as to reduce the contribution of particles coming from the sides of the sensor. In particular, the diameter of the first diode is smaller than that of the second diode. This was made possible thanks to the small aperture of the sensor. An illustration of the geometry of the low-energy proton sensor taking into account all the constraints discussed above is shown in Fig. 1.

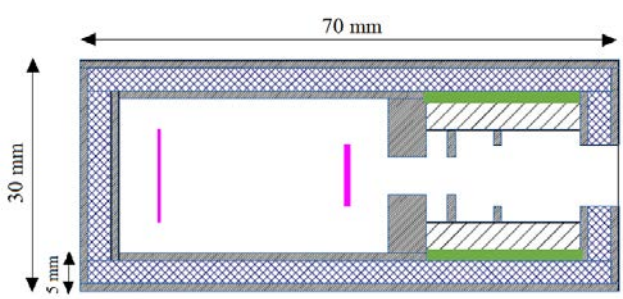

Fig. 1. Illustration of the geometry of the low-energy proton sensor. Aluminum is represented in grey, tungsten in blue, diodes in pink, steel strapping in green, and pieces of samarium-cobalt in hatched areas.

The front silicon diode (700 µm thick) has a sensitive area of 50 mm² while the back silicon diode (300 µm thick) has a sensitive area of 113 mm².

III. The Modeling of the Sensor

A. *Magnetic field calculation*

The magnet is composed of two samarium-cobalt pieces so that the magnetic field is oriented as indicated in Fig. 2. The height of the samarium-cobalt magnet is a compromise between the total volume of the sensor and the deflection of electrons.

The magnetic field of the samarium-cobalt magnet is calculated using PS-PERMAG software [14]. The vertical cross-section of this calculation is presented in Fig. 2.

Between the two pieces, the magnetic field is approximately uniform. At the center the magnetic field is equal to 0.36 T. These calculations do not take into account the steel strapping which will increase the intensity of the magnetic field between the two pieces and confine the magnetic field inside the sensor. Results of this magnetic field calculation are used in Monte-Carlo simulations to calculate response functions of the low-energy proton sensor.

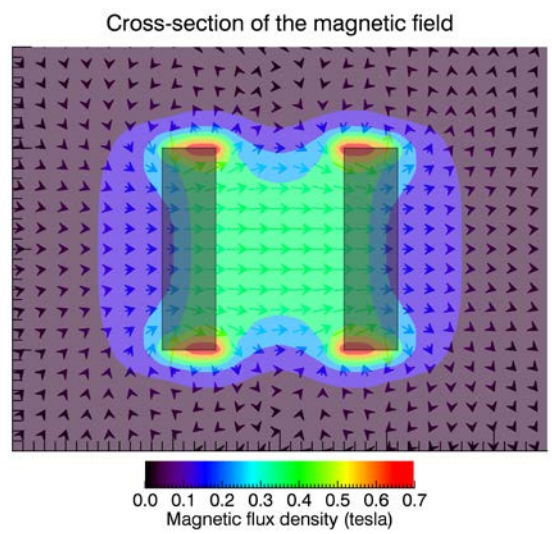

Fig. 2. Vertical cross-section of the magnetic field produced by the magnet.

B. *Monte-Carlo simulations*

Response functions of protons and electrons in anti-coincidence and coincidence modes of the low-energy proton sensor are computed from Monte-Carlo simulations based on the GEANT-4 ("GEometry ANd Tracking") toolkit [15] [16]. The geometry of the low-energy proton sensor is drawn and translated into GEANT-4 using FASTRAD Software [17]. In these simulations a spherical source with a radius equal to 4.5 *cm* is assumed (so that it surrounds the sensor) with a cosine-law angular distribution for velocity vector directions [18]. Five million tries are performed per incident energy. The efficiency of the sensor is simulated by calculating the GEF (GEometric Factor) which is obtained from the ratio between

the amount of particles detected per channel over the total number of particles launched per incident energy. Its expression is given in (1) and calculated using [18] and [19] where R is the radius of the source and N_{det} the amount of particles detected per channel.

$$GEF = 4\pi^2 R^2 \frac{N_{det}}{N_{Total}} \quad (1)$$

N_{det} represents the number of particles that deposit energy within the energy range of a given channel in the front diode only in anti-coincidence mode. For the coincidence mode it represents the number of particles that deposit energy in both diodes for which the mean of energies deposited in both diodes is in the energy range of a given channel. At the entrance of the sensor, an aluminum foil of 50 µm thickness is added for Monte-Carlo simulations to take into account the multi-layer insulation which will cover the instrument.

C. Numerical results

1) Response functions

Proton response functions in anti-coincidence and coincidence modes are shown in Fig. 3 and in Fig. 4 respectively.

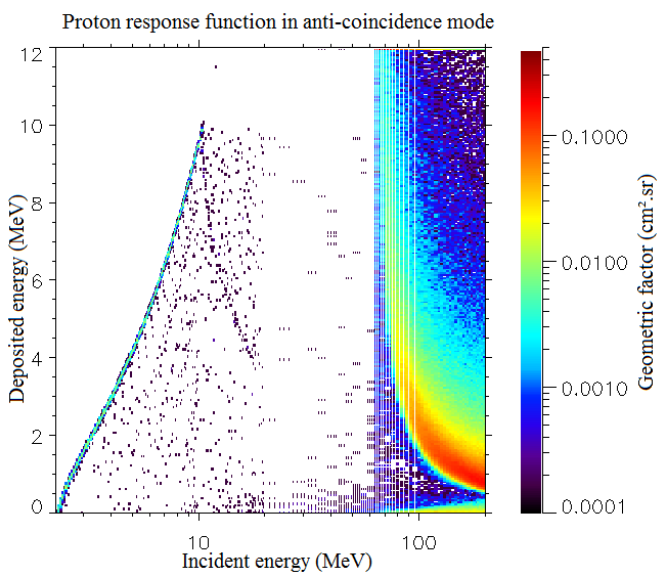

Fig. 3. Proton response function in anti-coincidence mode. Geometric factor (cm².sr) in incident energy (x-axis)-deposited energy (y-axis) map.

In Fig. 3 two regions can be highlighted: protons with incident energies lower than 12 MeV and protons with incident energies higher than 65 MeV. The first part is attributed to protons which are entering by the main aperture and deposit all their energy in the front diode of the sensor. The second part is attributed to protons which cross the shielding before reaching the front diode.

In Fig. 4 the response function indicates two regimes: protons with energies lower than 65 MeV which come from the aperture of the sensor and deposit energy in the two diodes, and protons with incident energies higher than 65 MeV which cross the shielding before reaching the two diodes.

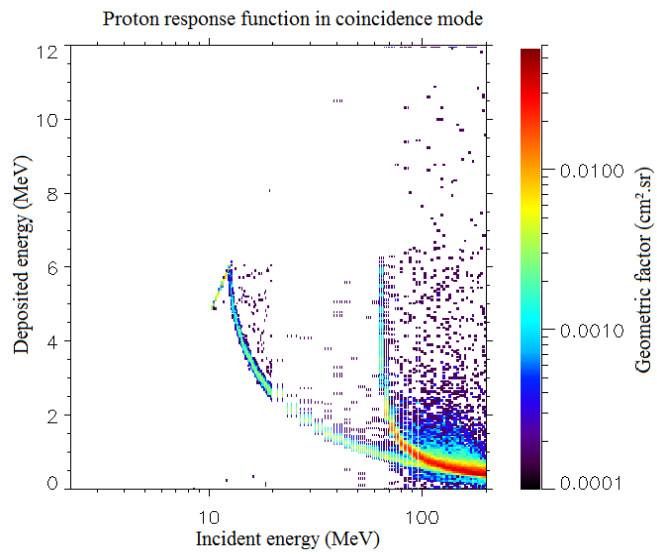

Fig. 4. Proton response function in coincidence mode. Geometric factor (cm².sr) in incident energy (x-axis)-deposited energy (y-axis) map.

With Fig. 3 and Fig. 4, 2-20 MeV protons are measured thanks to anti-coincidence and coincidence modes. Specifically, protons of 2-12 MeV are measured in anti-coincidence mode, and protons of 12-20 MeV are measured in coincidence mode. In the two cases, high-energy protons cross the shielding and are detected with a higher geometric factor than that of 2-20 MeV energy protons. Simulations were performed using the same number of particles for all incident energies. Nevertheless, in space fluxes of particles depend on the energy. High-energy proton fluxes are much lower than those of 2-20 MeV. A lower contribution from high-energy protons is then expected. Flux models will be taken into account in subsection III.C.2 to investigate the relative contribution of 2-20 MeV protons and higher energies. Note that to reduce even more the high-energy proton contribution larger thicknesses of tungsten are required.

Electron response functions in anti-coincidence and coincidence modes are shown in Fig. 5 and Fig. 6 respectively.

In Fig. 5 some electrons are detected in anti-coincidence mode. More precisely, they are mostly photons produced by Bremsstrahlung. If we compare with the geometric factor of protons in anti-coincidence mode, the one in the case of electrons is much lower. This is due to the magnet which deflects the major part of electrons. In addition, electrons deposit energies less than 2 MeV so some electrons will be detected only in the first channels.

In Fig. 6, a few electrons are detected in coincidence mode but with a very low geometric factor. Furthermore, for all these simulations (protons and electrons) no threshold has been taken into consideration to filter out low energy depositions (and electronic noise by the way). With a threshold set at 0.5 MeV for example, which is the case for the sensor A of ICARE-NG, only few electrons would be

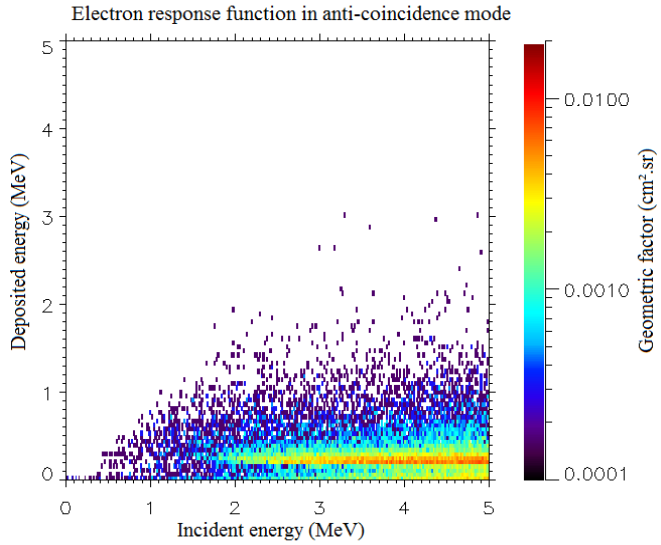

Fig. 5. Electron response function in anti-coincidence mode. Geometric factor (cm².sr) in incident energy (x-axis)-deposited energy (y-axis) map.

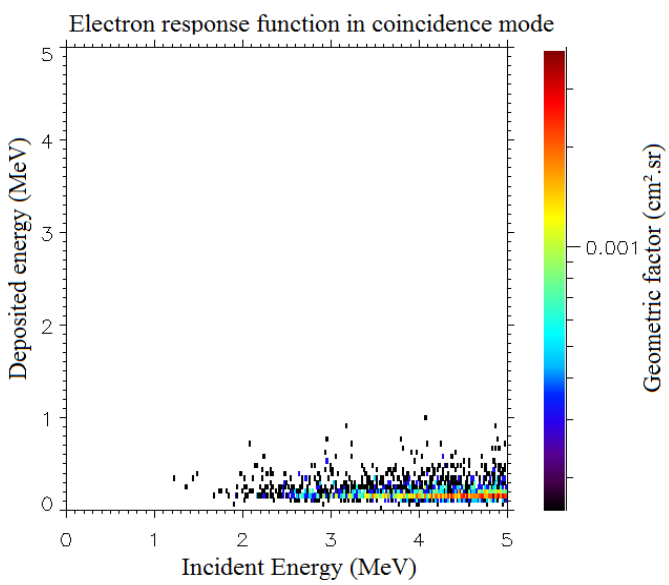

Fig. 6. Electron response function in coincidence mode. Geometric factor (cm².sr) in incident energy (x-axis)-deposited energy (y-axis) map.

detectable in anti-coincidence mode. These response functions characterize the efficiency of the sensor to measure protons and electrons, but do not take into consideration particle distributions expected in space. In subsection III.C.2, response functions and fluxes of particles are used to simulate particle counts that will be returned by the sensor.

2) The modeling of calculated counts of particles

Fluxes of particles depend strongly on the satellite's location in the radiation belts. To take into account the response functions of the sensor and particle distributions, expected count rates for each channel are computed. The expression of count rates for a given deposited energy channel is provided in (2) and extracted from [20].

$$C = \int_{\alpha_{local}} \int_{E} J(E, \alpha_{local}) \times GEF(E, \alpha_{local}) \times dE d\alpha_{local} \qquad (2)$$

where $GEF(E, \alpha_{local})$ and $J(E, \alpha_{local})$ are respectively the geometric factor and the unidirectional differential flux at a given incident energy and local pitch-angle. In a first step, particle fluxes will be considered isotropic at spacecraft locations so response functions computed from an isotropic source will be adopted. AP-8 and AE-8 models [21] [22] are considered to compute differential fluxes at several McIlwain L-parameter values, which are the distances expressed in Earth-radii of the apex of magnetic field lines. After [23] [24] and [25] a correction factor is applied to electron fluxes with energies greater than 800 keV at L < 2.5 returned by the AE-8 model: AE-8 fluxes are divided by a factor of 100 for $L < 2.5$ and for energies greater than 800 keV (in other words, electron fluxes with energies greater than 800 keV are negligible below L=2.5). Count rates are calculated for all deposited energy channels along the magnetic equator. Results obtained for the anti-coincidence mode are shown in Fig. 7.

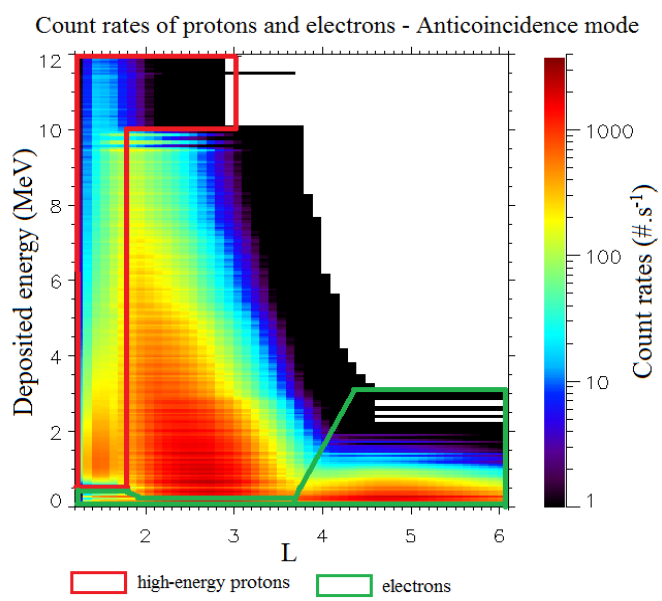

Fig. 7. Count rates of particles in McIlwain L-parameter (x-axis)-deposited energy (y-axis) map for the low-energy proton sensor in anti-coincidence mode.

Count rates obtained in Fig. 7 exhibit three regions. The first one with a red contour indicates count rates dominated by protons with energies greater than 65 MeV. The second one represented in green points out count rates dominated by energetic electrons. For the third one (with no specific contour) 2-12 MeV protons dominate count rates. To find out delimitations of each region, count rates of 2-12 MeV protons, protons with energies greater than 65 MeV, and electrons are plotted in three different intermediate figures. All the information is then grouped together in Fig. 7 where count rates of all particles detected in anti-coincidence mode are

taken into account.

For the coincidence mode, count rates for all deposited energy channels along the magnetic equator are illustrated in Fig. 8.

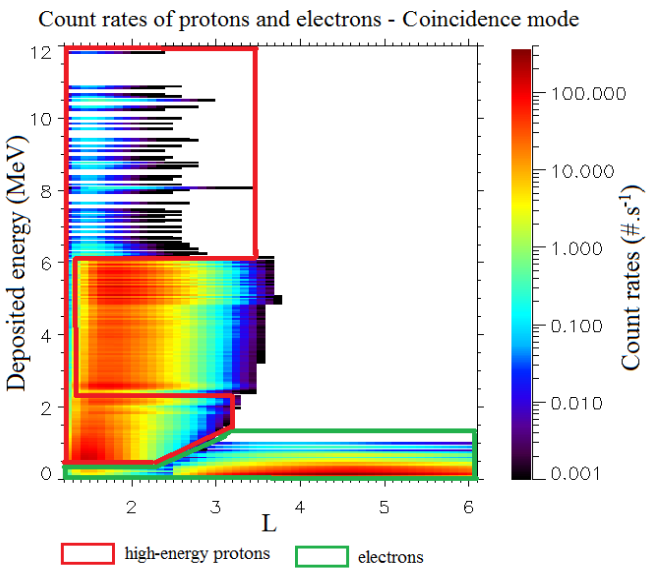

Fig. 8. Count rates of particles in McIlwain L-parameter (x-axis)-deposited energy (y-axis) map for the low-energy proton sensor in coincidence mode.

As for Fig. 7, count rates obtained in Fig. 8 exhibit three regions with high-energy protons for the one delimited by a red contour, electrons with the green contour, and the third one with 12-20 MeV protons with no specific contour.

As shown in Fig. 7 and in Fig. 8, 2-12 MeV protons are obtained in anti-coincidence mode and 12-20 MeV protons are detected in coincidence mode, even if the geometric factor of high-energy protons is much higher. The large difference in flux values of the two populations fully compensates the difference in the geometric factors. Note that some electrons will be measured in the low deposited energy channels but they will not interfere with the 2-20 MeV proton measurements, because they are not detected in the same channels or at the same L.

Clearly, the adopted sensor geometry allows discriminating 2-20 MeV protons accurately in a large radiation belt domain, and particularly allows sampling the peak flux. For $L < 1.7$ high-energy protons dominate count rates in anti-coincidence mode but their contribution cannot be easily removed since these protons cross the aluminum-tungsten-aluminum shielding. To limit even more their contribution the shielding has to be thicker. But design constraints to fit with the actual ICARE-NG radiation monitor make it difficult to increase again mass and volume of the low-energy proton sensor.

3) Predicted counts according to the pointing direction and the view angle

The results in III.C.2 are obtained by assuming an omnidirectional source. In this case, particles may reach the sensor from any direction. In particular, high-energy protons (E > 65 MeV) cross the shielding of the sensor because of their long range in the matter. For very low McIlwain L-parameter values (L < 1.5) the anisotropy is no more negligible. Due to the directionality of particles at low L values, fewer particles are expected than that predicted with the omnidirectional source. So, in this paper, a focus is given to the worst case to discriminate 2 to 20 MeV protons to other particles. However, protons of lower energies can only enter by the main entrance of the sensor. So, to go further, the view angle has to be taken into account as well as the pointing direction of the sensor according to the direction of the magnetic field.

According to the geometry of the low-energy proton sensor, the half angle of the aperture cone, β, is equal to 12.34°. In Fig. 9 the pointing direction, ω, of the sensor in respect to the local Earth magnetic field and its view angle at the magnetic equator are illustrated.

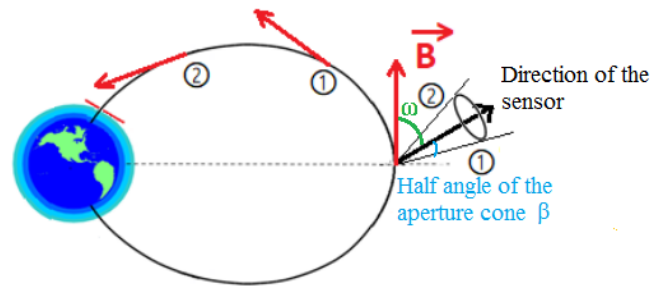

Fig. 9. The pointing direction and the half angle of the aperture cone of the sensor at the magnetic equator.

The points 1 and 2 represent respectively the mirror points of particles having an equatorial pitch-angle equal to ω+β and ω-β.

Considering Fig. 9, the flux at the entrance of the sensor is equal to the difference between the omnidirectional flux calculated at 1 and that calculated at 2. To this end, omnidirectional fluxes at the mirror points of particles having an equatorial pitch-angle of ω+β and ω-β have to be calculated. Omnidirectional fluxes at the mirror points 1 and 2, respectively named J_{omni1} and J_{omni2}, are given in (3).

$$J_{omni1,2} = \int_{\theta=-\beta}^{+\beta} \int_{\alpha=0}^{\pi} J_{uni1,2} \times \sin(\alpha) \times d\alpha \times d\theta \qquad (3)$$

In addition, the unidirectional flux is equal to the AP-8 flux divided by 4π. Finally, the flux at the entrance of the sensor is given in (4) where β is expressed in degrees and J_{omni1_AP8} and J_{omni2_AP8} are omnidirectional fluxes given by AP-8.

$$J_{detector} = \frac{\beta}{180} \times \left(J_{omni1\_AP8} - J_{omni2\_AP8}\right) \qquad (4)$$

Particle counts are calculated for protons in coincidence and anti-coincidence modes by using omnidirectional flux for high-energy protons and flux given in (4) for protons with an

energy lower than 65 MeV. For electrons, omnidirectional fluxes are assumed since their paths are not linear due to the scattering. Predicted counts by taking into account the view angle are given in Fig. 10 for the anti-coincidence and the coincidence modes for three different inclinations of the sensor with respect to the direction of the magnetic field: 0°, 30°, and 75°.

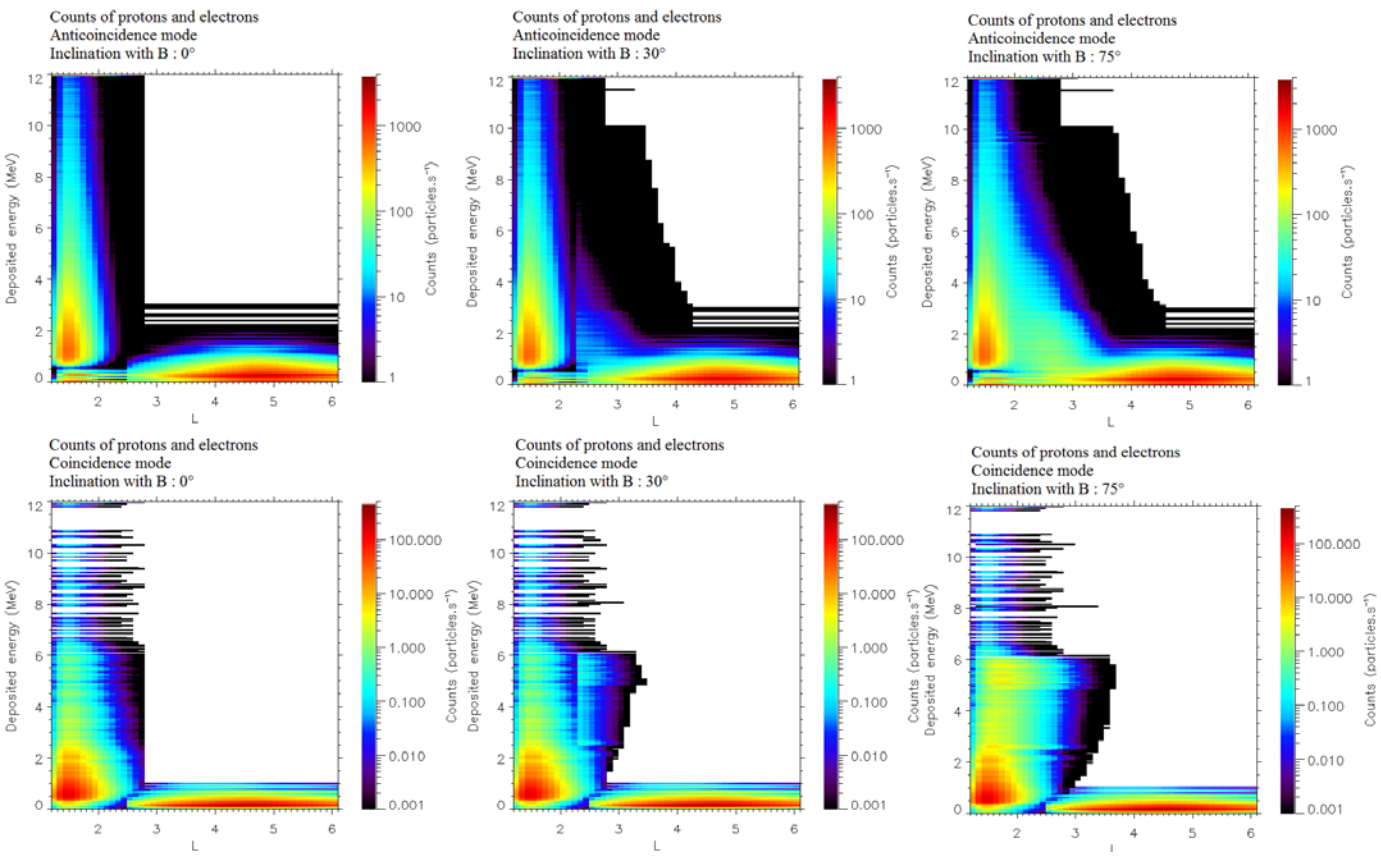

Fig. 10. Predicted counts of protons and electrons in anticoincidence mode at the top and in coincidence mode at the bottom for inclinations with the magnetic field of 0°, 30°, and 75° from the left to the right. The view angle is taken into account.

According to Fig. 10, low-energy protons are not measured when the direction of the sensor is aligned with the direction of the magnetic field (inclination of 0°). In this case, the main aperture of the sensor points toward the loss-cone. There, low-energy protons are not trapped by the magnetic field of the Earth because they precipitate into the upper atmosphere: as a result low-energy proton fluxes are then negligible. Due to the strong directionality of the sensor at low energies, the higher the inclination with respect to the direction of the magnetic field (close to 90°) is, the higher the counts of low-energy protons will be. This analysis highlights the importance to place the sensor in a direction approximately perpendicular to the direction of the magnetic field to maximize the low-energy protons' contribution to the count rates with respect to other particle distributions due to the strong directionality of the sensor at those energies.

4) Saturation, total counts, and drift

The ICARE-NG instrument is composed of 3 sensors and their associated electronics. When a particle deposits energy in a diode, this creates electron-hole pairs. The quantity of electron-hole pairs created is proportional to the energy deposited by the particle in the silicon diode. A potential is applied to the electrodes to collect these charges in order to know the energy deposited by the particle. It is important to have electronics that collect charges very quickly. If two particles deposit energy almost at the same time, charges created by the two particles in the silicon diode will be collected and related to a single particle which would have deposited energy equal to the sum of the energies of the two particles. This deposited energy will be that of the association of the two particles because the electronics is not able to separate the signal of the two particles if they deposit energy almost at the same time. This would falsely indicate a single particle with a deposited energy equal to the sum of the energies of the two particles. This effect is called analogic saturation or stack phenomenon.

For the electronics of the ICARE-NG instrument, the total counts over all channels may not exceed 200,000 particles per second to avoid this effect. Total counts are calculated in Fig. 11 and in Fig. 12 respectively for the anti-coincidence and for the coincidence modes for the low-energy proton sensor for an inclination of 75° with the direction of the magnetic field without taking into account a threshold for deposited energies. This is done by virtually flying the sensor in AP-8 and AE-8

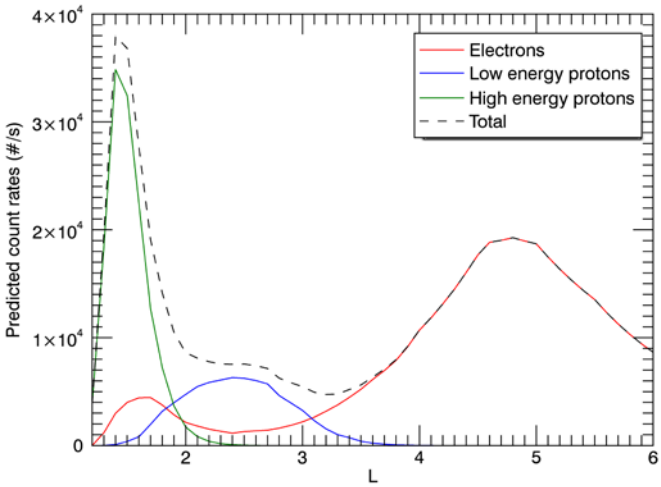

Fig. 11. Predicted count rates for the anti-coincidence mode for electrons (in red), low-energy protons (in blue), high-energy protons (in green), and the total count rates (in black).

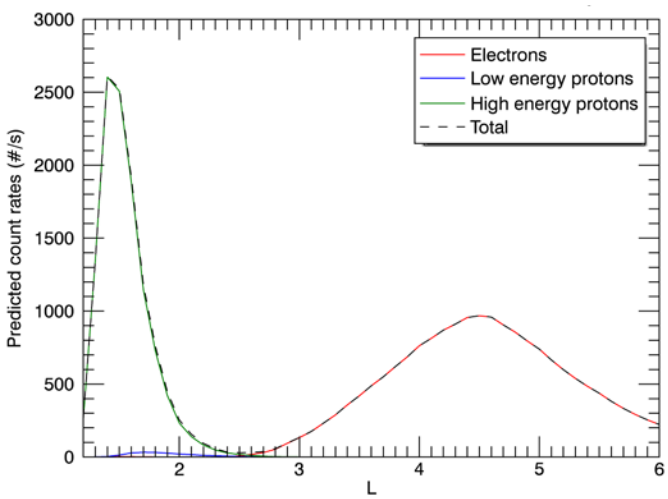

Fig. 12. Predicted count rates for the coincidence mode for electrons (in red), low-energy protons (in blue), high-energy protons (in green), and the total count rates (in black).

models along the magnetic equator.

For the coincidence and the anti-coincidence modes, according to Monte-Carlo simulations and the AE-8 and AP-8 models, the analogic saturation will not occur. In addition, large margins are taken (total counts do not exceed 40,000 while pile-up is observed for total counts higher than 200,000) because these results are obtained thanks to fluxes at the magnetic equator given by the AP-8 and AE-8 models. Fluxes that will be encountered in orbit may not be exactly those given by these models.

Furthermore, even if counts of low-energy protons are much lower than those of high-energy protons in coincidence mode they are not registered in the same channels so they will be detected. Concerning the anti-coincidence mode, since low-energy count rates are sufficient and that they are not registered in the same channels as for high-energy protons and electrons, good measurements of low-energy protons in anti-coincidence mode will be performed. Moreover, the default acquisition period will be set to 16 seconds with 14 seconds for the acquisition and 2 seconds of processing. So, considering predicted counts, they will be multiplied by a factor of 14 due to the acquisition time.

Due to the displacement damage in the diode, charge collection efficiency may decrease significantly for a long duration mission. So far, there is no measurement of the leakage current in the low-energy proton sensor to monitor the drift; this measurement is only implemented in sensor B. Note that this low-energy proton sensor was firstly designed to be implemented on electric orbit raising satellite to GEO (geostationary orbit). In a first step, it was assumed that the rising phase to GEO is not long enough to significantly degrade the diodes. Moreover, the multi-layer insulation filters protons with energies lower than 2.5 MeV, which limits the increase of the leakage current.

5) Compromises for the geometry of the sensor

Fig. 13 illustrates the electron response function in anti-coincidence mode obtained without taking into account the magnet.

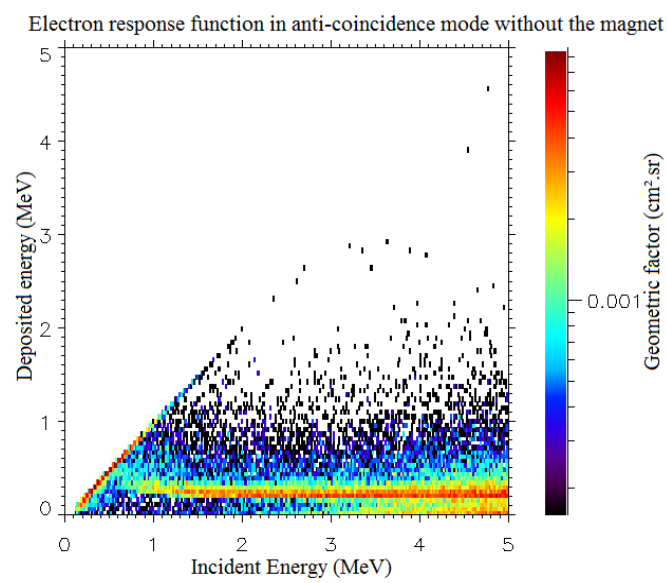

Fig. 13. Electron response function in anti-coincidence mode without the magnet. Geometric factor (cm².sr) in incident energy (x-axis)-deposited energy (y-axis) map.

Electrons with incident energies lower than 2 MeV impact channels for deposited energies lower 2 MeV. These electrons, which are above the threshold set at 0.5 MeV, contaminate low-energy proton measurements which are detected in the same channels and with a geometric factor of the same order of magnitude. Thanks to the magnet (cf. Fig. 5), these electrons are deflected before they could reach the front diode, and the contribution of other electrons is minimized which allows good measurements of low-energy protons. The use of the magnet adds constraints (weight, steel strapping…), but it is necessary to ensure a good quality of low-energy proton measurements.

The other compromise was the use of the tungsten

shielding. If the shielding was only made of aluminum, protons with energies higher than 30 MeV would cross the shielding. Thanks to the tungsten, only protons with energies higher than 65 MeV cross the shielding which minimizes the contribution of high-energy protons. To shift this limit to 100 MeV for example, the thickness of tungsten should be around 8 mm, which doubles the mass of the sensor. For our needs, the best compromise was to choose to stop protons with energy lower than 65 MeV to minimize the contribution of high-energy protons and at the same time for keeping a volume and a mass for the sensor compatible with the ICARE-NG instrument.

Diameter of the diodes is also a critical choice. Response function for protons in anti-coincidence mode with a diameter for the first diode equal to that of the second diode is illustrated in Fig. 14.

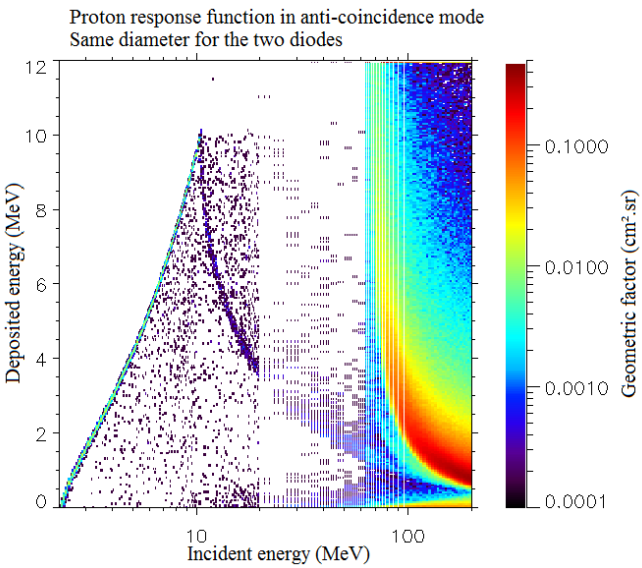

Fig. 14. Proton response function in anti-coincidence mode for the same diameter for the two diodes. Geometric factor (cm².sr) in incident energy (x-axis)-deposited energy (y-axis) map.

When the first diode has the same diameter as the second diode, much more high-energy protons are detected in all channels. Indeed, the amount of low-energy protons detected does not change, but the amount of high-energy protons detected is much higher because the surface of the diode exposed to those protons is larger. In our case, to reduce the contribution of high-energy protons, the diameter of the first diode was chosen to be smaller than that of the second diode.

IV. Manufacturing and Tests

This paper presents numerical results of the low-energy proton sensor, which is in production at EREMS [26]. An engineering model of the new version of the ICARE-NG instrument will be delivered in spring 2020. The geometry of the new version of the instrument is illustrated in Fig. 15.

Tests with radioactive sources are planned to perform calibrations of the three sensors and also to validate the

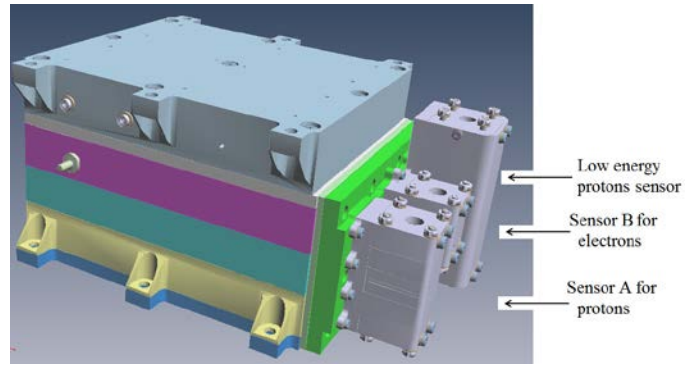

Fig. 15. Geometry of the new version of the ICARE-NG instrument. Picture given by EREMS.

efficiency of the magnet to deflect the major part of electrons in the low-energy proton sensor. These tests will be performed at ONERA-DPHY in a vacuum chamber. Calibrations will be made using a tri-isotope source (Plutonium, Americium, and Curium) and a Californium source to determine the correspondence between deposited energy channel number and the energy deposited by particles. A Strontium source, which emits a continuous spectrum of electrons, will be used to validate the magnet geometry and intensity.

The new version of the ICARE-NG instrument which includes the low-energy proton sensor will be on-board several satellites for which launches are expected to be in 2021, so flight models of the instrument will be delivered in 2020.

New measurements will be performed with this new version of ICARE-NG over a large range of energy for protons and electrons. The previous version of the ICARE-NG instrument was equipped with the sensors A, B, and C. The new version of the ICARE-NG instrument is equipped with the sensors A and B, and for the third sensor either the low-energy proton sensor or the sensor C can be chosen according to the needs of the mission. Table I illustrates expected differential and integrated channels.

The low-energy proton sensor allows extending capabilities of the ICARE-NG instrument to low-energy protons, which are not widely studied. Also, as the sensor A and the low-energy proton sensor are both sensitive to protons with energies higher than 12.9 MeV, cross-calibrations will be performed. In addition, measurements of high-energy protons will also be provided by the low-energy proton sensor, but that is not illustrated in the Table I since we need to have the complete description of the satellite to characterize these high energy contributions accurately.

V. Conclusion

A new sensor of low-energy protons has been designed. This sensor is compatible with the existing ICARE-NG instrument and can replace the sensor C according to the needs. Monte-Carlo simulations have been performed to calculate response functions of the sensor. By combining response functions calculated with GEANT-4 and particle fluxes given by the AP-8 and AE-8 models, predicted count

TABLE I
PROTON AND ELECTRON MEASUREMENTS FOR THE SENSORS A, B, AND C, AND THE LOW-ENERGY PROTON SENSOR.

Sensor A		Sensor B		Sensor C		Low-energy proton sensor
e- (MeV)	p (MeV)	e- (MeV)	p (MeV)	e- (MeV)	p (MeV)	p (MeV)
>0.87	12.9	>0.249	>80	>2.68	31	2.5
>0.93	18.6	>0.270	>85	>2.77	47.3	3.0
>0.986	63	>0.299	>95	>2.85	61	3.5
>1.078	65	>0.320	>105	>2.93	64	4.0
>1.135	69	>0.342	>115	>3.01	67	4.5
>1.226	74	>0.363	>130	>3.09	75	5.0
>1.3	81	>0.384	>160	>3.17	80	5.5
>1.359	90	>0.413	>190	>3.25	85	6.0
>1.508	100	>0.455			90	7.0
>1.657	115	>0.505			100	8.0
>1.823	>54	>0.554			>56	9.0
>1.974	>60	>0.604			>60	10.0
>2.106	>66	>0.653			>65	12.0
>2.254	>73	>0.703			>70	14.0
>2.404	>81	>0.752			>75	16.0
>2.567	>90	>0.802			>80	18.0
	>100	>0.895			>90	20.0
	>110	>0.994			>100	22.0
		>1.093				24.0
		>1.192				30.0

rates have been calculated. Sensor performances indicate that the sensor is sensitive to 2-12 MeV protons for $1.7 < L < 3.5$ in anti-coincidence mode and to 12-20 MeV protons for $1.2 < L < 3.5$ in coincidence mode, and it is also sensitive to high-energy protons for L < 1.7 and to electrons for L > 3.3. This sensor allows measurements of a wide range of energy for protons and also measurements of electrons depending on the location of the satellite in radiation belts, including measurements of low-energy protons which are very important to complete empirical or physical models of the Earth's radiation belts since they are not widely studied by other radiation monitors.

REFERENCES

[1] S. Bourdarie and D. Boscher, "Space radiation environment," in *Space Radiation Environment and its Effects on Spacecraft Components and Systems SREC04*, Toulouse: Cépaduès, 2004, pp. 57-82.

[2] D. N. Baker, "The occurrence of operational anomalies in spacecraft and their relationship to space weather," *IEEE Trans. Nucl. Sci.*, vol. 28, no. 6, pp. 2007–2016, Dec. 2000.

[3] D. Boscher *et al.*, "In Flight Measurements of Radiation Environment on Board the French Satellite JASON-2," *IEEE Trans. Nucl. Sci.*, vol. 58, no. 3, pp. 916–922, Jun. 2011.

[4] D. Boscher *et al.*, "In-Flight Measurements of Radiation Environment on Board the Argentinean Satellite SAC-D," *IEEE Trans. Nucl. Sci.*, vol. 61, no. 6, pp. 3395–3400, Dec. 2014.

[5] D. N. Baker *et al.*, "The Relativistic Electron-Proton Telescope (REPT) Instrument on Board the Radiation Belt Storm Probes (RBSP) Spacecraft: Characterization of Earth's Radiation Belt High-Energy Particle Populations," in *The Van Allen Probes Mission*, N. Fox and J. L. Burch, Eds. Boston, MA: Springer US, 2014, pp. 337–381.

[6] M. S. Gussenhoven, E. G. Mullen, and D. H. Brautigam, "Improved understanding of the Earth's radiation belts from the CRRES satellite," *IEEE Trans. Nucl. Sci.*, vol. 43, no. 2, pp. 353–368, Apr. 1996.

[7] K. Yando, R. M. Millan, J. C. Green, and D. S. Evans, "A Monte Carlo simulation of the NOAA POES Medium Energy Proton and Electron Detector instrument: TECHNIQUE," *J. Geophys. Res.*, vol. 116, no. A10, Oct. 2011.

[8] Y. Sasaki, H. Matsumoto, T. Goka, T. Nakamura, K. Terasawa, and H. Kitamura, "Technical data acquisition equipment for GOSAT," in *Proc. 30th Int. Cosmic Ray Conf. (ICRC)*, 2007, pp. 643–646.

[9] J. L. Burch, and V. Angelopoulos, "The THEMIS Mission," Springer, Space Science Reviews, Volume 141, Issues 1–4, 2008, pp. 5–34.

[10] D. G. Mitchell *et al.*, "Radiation Belt Storm Probes Ion Composition Experiment (RBSPICE)," in *The Van Allen Probes Mission*, N. Fox and J. L. Burch, Eds. Boston, MA: Springer US, 2014, pp. 263–308.

[11] J. B. Blake et al., "The Magnetic Electron Ion Spectrometer (MagEIS) Instruments Aboard the Radiation Belt Storm Probes (RBSP) Spacecraft," in *The Van Allen Probes Mission*, N. Fox and J. L. Burch, Eds. Boston, MA: Springer US, 2014, pp. 383–421.

[12] D. Falguere *et al.*, "In-flight observations of the radiation environment and its effects on devices in the SAC-C polar orbit," *IEEE Trans. Nucl. Sci.*, vol. 49, no. 6, pp. 2782–2787, Dec. 2002.

[13] P. Vaze, S. Neeck, W. Bannoura, J. Green, A. Wade, M. Mignogno, G. Zaouche, V. Couderc, E. Thouvenot, and F. Parisot. "The Jason-3 Mission: Completing the transition of ocean altimetry from research to operations," in *Sensors, Systems, and Next-Generation Satellites XIV*, vol. 7826, p. 78260Y, International Society for Optics and Photonics, 2010.

[14] "PS-PERMAG Capabilities." [Online]. Available: http://www.permagsoft.com/english/ps-permag.html. [Accessed: 19-Mar-2019].

[15] S. Agostinelli *et al.*, "Geant4—a simulation toolkit," *Nucl. Instrum. Methods Phys. Res. A, Accel. Spectrom. Detect. Assoc. Equip.*, vol. 506, no. 3, pp. 250–303, Jul. 2003.

[16] J. Allison *et al.*, "Geant4 developments and applications," *IEEE Trans. Nucl. Sci.*, vol. 53, no. 1, pp. 270–278, Feb. 2006.

[17] "FASTRAD Software for Space radiation analysis," *FASTRAD Software*. [Online]. Available: https://www.fastrad.net/. [Accessed: 10-Sep-2019].

[18] "Normalisation modelling sources," [Online]. Available: http://geant4.in2p3.fr/2007/prog/GiovanniSantin/GSantin _Geant4_Paris07_Normalisation_v07.pdf. [Accessed: 10-Sep-2019].

[19] J. D. Sullivan, "Geometric factor and directional response of single and multi-element particle telescopes," *Nucl. Instrum. Methods*, vol. 95, no. 1, pp. 5–11, Aug. 1971.

[20] M. Ruffenach, S. Bourdarie, J. Mekki, D. Falguere, and J. R. Vaille, "Proton Radiation Belt Anisotropy as Seen by ICARE-NG Head-A," *IEEE Trans. Nucl. Sci.*, vol. 66, no. 7, pp. 1753–1760, Jul. 2019.

[21] D. M. Sawyer and J. I. Vette, "AP-8 Trapped Proton Environment for Solar Maximum and Solar Minimum," *NSSDC WDC-A-R&S 76-06*, Dec. 1976.

[22] J. I. Vette, "The NASA/National Space Science Data Center Trapped Radiation Environment Model Program (1964- 1991)," *NSSDC/WDC-A-R&S 91-29*, Nov. 1991.

[23] D. Boscher, S. Bourdarie, V. Maget, A. Sicard-Piet, G. Rolland, and D. Standarovski, "High-Energy Electrons in the Inner Zone," *IEEE Trans. Nucl. Sci.*, vol. 65, no. 8, pp. 1546–1552, Aug. 2018.

[24] J. F. Fennell *et al.*, "Van Allen Probes show that the inner radiation zone contains no MeV electrons: ECT/MagEIS data," *Geophys. Res. Lett.*, vol. 42, no. 5, pp. 1283–1289, Mar. 2015.

[25] A. Sicard, D. Boscher, S. Bourdarie, D. Lazaro, D. Standarovski, and R. Ecoffet, "GREEN: the new Global Radiation Earth ENvironment model (beta version)," *Ann. Geophys.*, vol. 36, no. 4, pp. 953–967, Jul. 2018.

[26] "EREMS is a company specialized in the design and the realization of electronic equipments, and of associated softwares." [Online]. Available: http://www.erems.fr/en/. [Accessed: 22-Jul-2019].